Electronic Supplementary Material (ESI) for Nanoscale.

Supporting Information

Synergistic oxygen substitution and heterostructure construction in polymeric semiconductors for efficient water splitting

Li Chen, [a] *Yuze Wang,* [a] *Chongbei Wu,* [a] *Guanhang Yu,* [a] *Yue Yin,* [a] *Chenliang Su,* [b] *Jijia Xie,* [d]
*Qing Han,** [a] *Liangti Qu*[c]

[a]Key Laboratory of Photoelectronic/Electrophotonic, Conversion Materials, Key Laboratory of Cluster Science, Ministry of Education, School of Chemistry and Chemical Engineering, Beijing Institute of Technology, Beijing 100081, China.
*Correspondence author: qhan@bit.edu.cn

[b]SZU-NUS Collaborative Center and International Collaborative Laboratory of 2D Materials for Optoelectronic Science and Technology of Ministry of Education, College of Optoelectronic Engineering, Shenzhen University, Shenzhen 518060, China

[c]Department of Chemistry, Tsinghua University, Beijing 100081, China.

[d]Department of Chemical Engineering, University College London, Torrington Place, London, WC1E 7JE, United Kingdom.

Experimental Section

Chemical reagent: Dicyandiamide (DCDA), formic acid (HCOOH, 88%), lithium chloride (LiCl, 97%), potassium chloride (KCl, 99.5%) were purchased from Sigma-Aldrich and used without further purification.

Synthesis of TOH-CN: We prepared the TOH-CN samples, drawing on the synthesis methods from the literatures.[1,2] In general, a homogeneous dispersion of formic acid and DCDA (0.05 g/mL) with stoichiometry ratio of 0.4:1 was dissolved in 40 ml deionized water, heated and stirred at 130 ºC for 6h, and then dried overnight. Subsequently, the above resulting white crystalline precursor was dispersed throughout 12 mL of deionized water, and then kept in liquid nitrogen to form a white monolith assembly. 1g of the white assembly was added into the eutectic mixture of lithium chloride (4.5g) and potassium chloride (5.05g), and the mixture was uniformly grinded. The mixture was wrapped in an ampule glass bottle, and then heated at 400 ℃ with a ramp rate of 6 ℃ min^{-1} in N_2 flow, then cooled to room temperature. Next, the ampule was evacuated and sealed in high temperate, followed by heating at 600 ℃ with a ramp rate of 1 ℃ min^{-1} and stabilized for 16 h. After cooling to room temperature, the obtained sample was repeatedly washed with boiling water to remove residual salt. The effect of the oxygen content on the photocatalytic performance of obtained samples is investigated by adjusting stoichiometry ratio of formic acid to DCDA (from 0.2, 0.4 and 0.5 to 0.7).

Synthesis of T-CN: 1g of DCDA was directly mixed with an eutectic mixture of LiCl (4.5g) and KCl (5.05g), and was uniformly grinded in a glovebox. The mixture was then wrapped in an ampule glass bottle, and heated at 400 ℃ with a ramp rate of 6 ℃ min^{-1} in N_2 flow, followed by cooling to room temperature. The ampule was evacuated and sealed in high temperate, followed by heating at 600 ℃ with a ramp rate of 1 ℃ min^{-1} and stabilized for 16 h. After cooling to room temperature, the obtained sample was repeatedly washed with boiling water to remove residual salt.

Synthesis of OH-CN: A homogeneous dispersion of formic acid and DCDA (0.05 g/mL) with stoichiometry ratio of 0.4:1 was heated and stirred at 130 ºC for 6h, and then dried overnight. Subsequently, the above resulting white crystalline precursor was directly heated at 550 ℃ with a ramp rate of 5 ℃ min^{-1} and stabilized for 4 h.

Synthesis of g-C_3N_4 : The original g-C_3N_4 was prepared by direct thermal polymerization of DCDA at 550 ℃ with a heating rate of 5 ℃/min in N_2 atmosphere, and stabilized for 4 h.

Characterization. The morphology of samples was observed by scanning electron microscopy (SEM, JSM-7500) and transmission electron microscopy (TEM, 7650B, Hitachi). Power X-ray diffraction (PXRD) patterns were taken using a 1710 diffractometer from Netherlands equipped with a Cu Kα irradiation source (λ=1.54 Å). Fourier transform infrared (FTIR) spectra was recorded by a Bruker spectrometer (Equinox 55/S) in the wavenumber range of 500-4000 cm^{-1}. The UV-Vis absorption spectra was performed on a 2600pc spectrophotometer using $BaSO_4$ as reflectance. XPS measurements were carried out on an ESCALab220i-XL electron spectrometer from VG Scientific, using 300 W Al Ka radiation. The solid-state ^{13}C CP-MAS nuclear magnetic resonance (NMR) spectra were surveyed on a JNM-ECZ600R spectrometer.

Photocatalytic tests. The photocatalytic properties of the as-prepared products were measured by the half reactions of water reduction and oxidation, which was operated in a closed top-irradiation vessel using a 300 W Xeon-lamp source to irradiate. For the photocatalytic hydrogen evolution reaction (HER), 30 mg of photocatalysts with 3 wt% H_2PtCl_6 cocatalysts was dispersed in an aqueous solution (100 ml) containing methanol (10 vol %) as electron donor. For the photocatalytic oxygen evolution reaction (OER), 30 mg of photocatalysts loaded CoO_x (obtained by the photodeposition method) [3] as cocatalysts was added to 100 mL of solution including $NaIO_3$ as electron acceptor. The reaction solution was evacuated about 1h to remove air prior to irradiation. The amount of evolved H_2 and O_2 was measured by gas chromatography (GC-7900) with high-purity Ar gas flow. Apparent quantum yield (AQY) was calculated by using the following formula:

$$AQY(\%) = \frac{2 \times the\ number\ of\ evolved\ hydrogen\ molecules}{The\ number\ of\ incident\ photons} \times 100\%$$

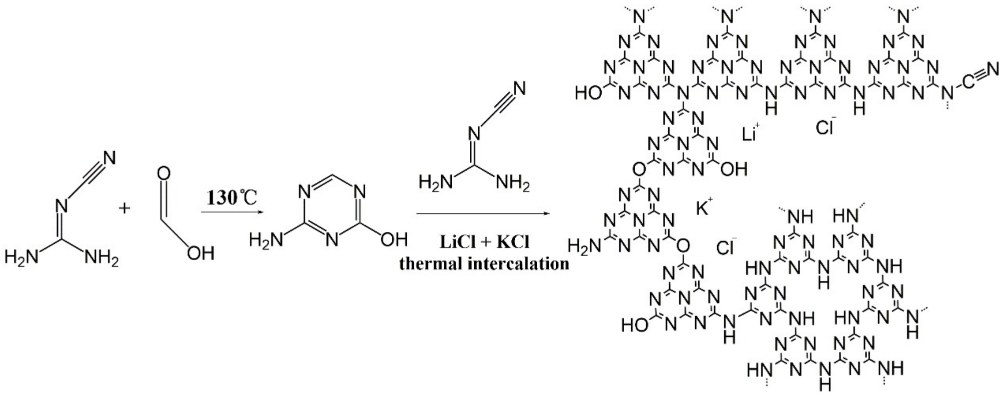

Scheme S1. The synthetic process for the TOH-CN.

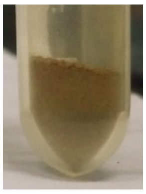

Figure S1. Photographs of TOH-$CN_{0.4}$.

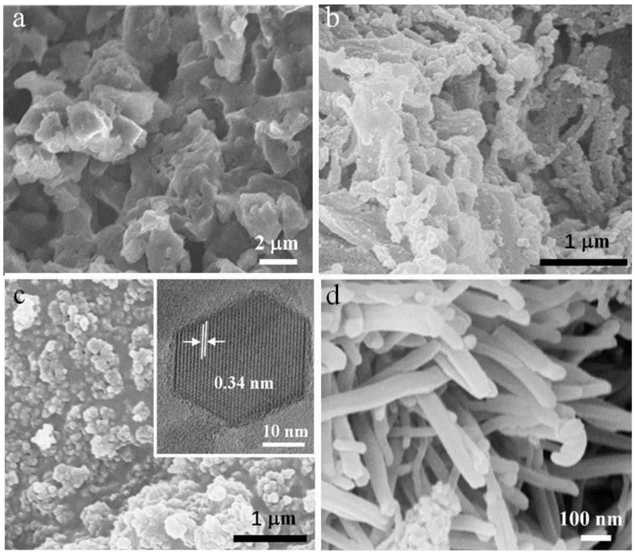

Figure S2. SEM images of (a) g-C_3N_4, (b) OH-CN, (c) T-CN (Inset: HR-TEM image of T-CN) and (d) TOH-$CN_{0.4}$.

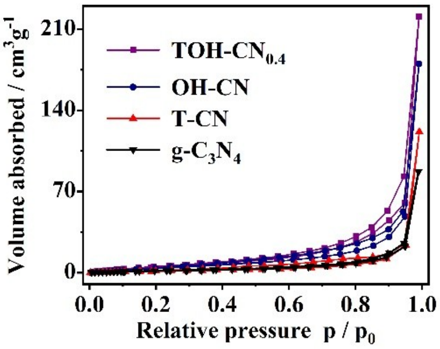

Figure S3. N_2 adsorption isotherms of g-C_3N_4, T-CN, OH-CN, TOH-$CN_{0.4}$.

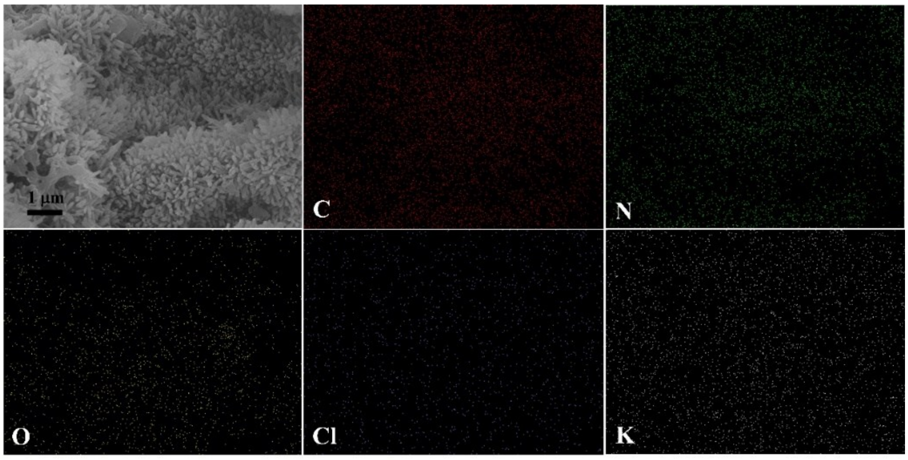

Figure S4. SEM image and the corresponding EDX element mappings of the TOH-$CN_{0.4}$, showing the distribution of C, N, O, Cl, K.

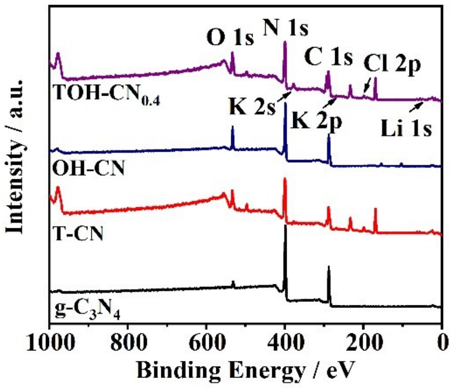

Figure S5. High-resolution X-ray photoelectron spectra for the g-C_3N_4, OH-CN, T-CN, TOH-$CN_{0.4}$.

Table S1. The relative N species concentration (%) from XPS spectra of N1s.

Sample	N1(%)	N2(%)	N3(%)	N1/N2	Bandgap(eV)
g-C_3N_4	66.1	14.5	19.4	4.5	2.57
TOH-$CN_{0.4}$	63.0	16.7	20.3	3.8	2.24

Table S2. The relative element percentages (at%) of g-C_3N_4, TOH-$CN_{0.4}$ from XPS spectra.

Samples	C (at%)	N (at%)	C/N	O (at%)
g-C_3N_4	40.70	57.37	0.71	1.93
TOH-$CN_{0.4}$	42.67	53.19	0.80	4.14

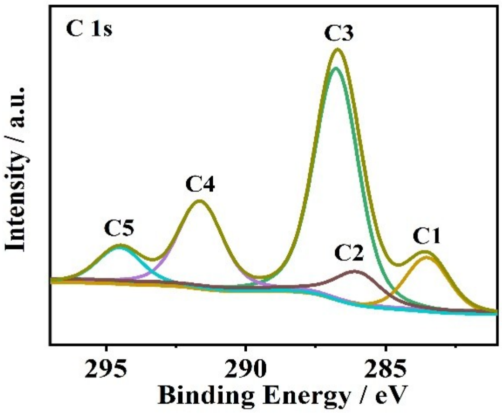

Figure S6. The high-resolution C1s peak of the TOH-$CN_{0.4}$.

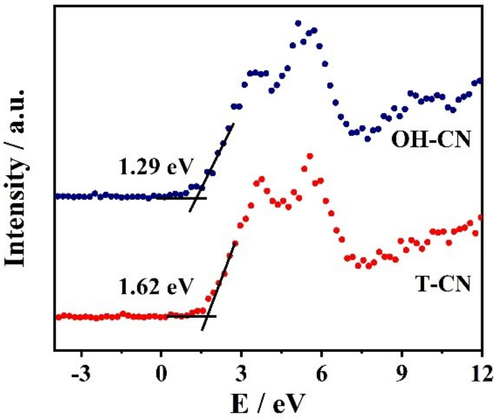

Figure S7. Valence band (VB) spectra of of the T-CN and OH-CN.

Table S3. The relative element percentages (at%) of T-CN, TOH-CN$_{0.2}$, TOH-CN$_{0.4}$, TOH-CN$_{0.5}$, TOH-CN$_{0.7}$ from EDS spectra.

Samples	C (at.%)	N (at.%)	O (at.%)
T-CN	42.85	55.07	2.08
TOH-CN$_{0.2}$	42.98	54.25	2.77
TOH-CN$_{0.4}$	42.56	53.23	4.21
TOH-CN$_{0.5}$	42.04	52.08	5.88
TOH-CN$_{0.7}$	41.45	51.41	7.24

A series of TOH-CN samples were synthesized where the weight ratio of formic acid to dicyandiamide was varied, with values of 0.2, 0.4, 0.5 and 0.7, which were named TOH-CN$_{0.2}$, TOH-CN$_{0.4}$, TOH-CN$_{0.5}$ and TOH-CN$_{0.7}$, respectively. As shown in Table S3, with increase of the weight ratio of formic acid to dicyandiamide, the oxygen content in the TOH-CN samples increases gradually from TOH-CN$_{0.2}$, TOH-CN$_{0.4}$, TOH-CN$_{0.5}$, to TOH-CN$_{0.7}$.

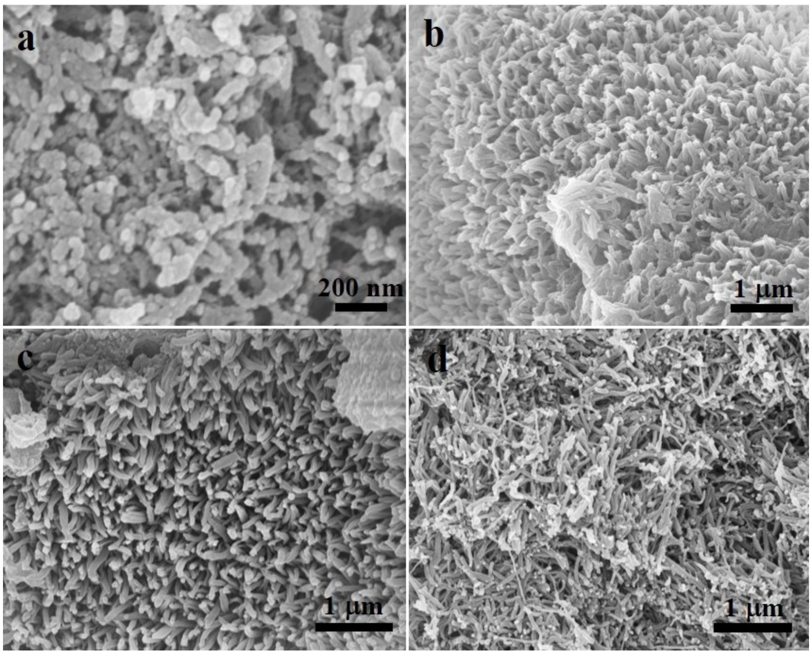

Figure S8. SEM images of (a) TOH-CN$_{0.2}$, (b) TOH-CN$_{0.4}$, (c) TOH-CN$_{0.5}$, (d) TOH-CN$_{0.7}$.

Interestingly, the nanoribbon morphology can be easily controlled by adjusting the weight ratio of formic acid to dicyandiamide. The TOH-CN$_{0.2}$ showed nanoparticle morphology with a grain size of ten nanometers **(Figure S8a)**. The increase of weight ratio of formic acid to dicyandiamide led to the generation of nanoribbon morphologies for the TOH-CN$_{0.4}$ **(Figure S8b)**, TOH-CN$_{0.5}$ **(Figure S8c)** and TOH-CN$_{0.7}$ **(Figure S8d)**. As we can see, the increasing oxygen content in the TOH-CN samples was thinning the nanoribbons from TOH-CN$_{0.4}$, TOH-CN$_{0.5}$ to TOH-CN$_{0.7}$.

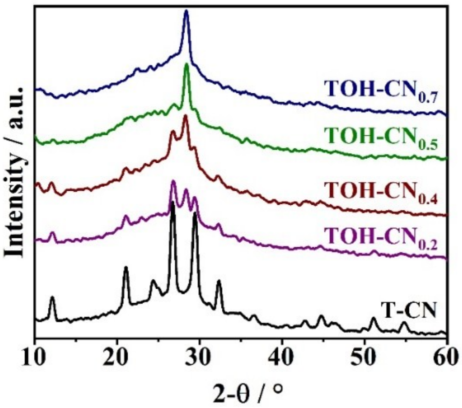

Figure S9. XRD patterns of T-CN, TOH-CN$_{0.2}$, TOH-CN$_{0.4}$, TOH-CN$_{0.5}$, TOH-CN$_{0.7}$.

As shown in Figure S9, the increase of the oxygen content in the TOH-CN samples results in increased amorphous structure from T-CN, TOH-CN$_{0.2}$, TOH-CN$_{0.4}$, TOH-CN$_{0.5}$ to TOH-CN$_{0.7}$, indicating a low degree of polymerization, which can be attributed to the increase of oxygen substitution (Table S3).

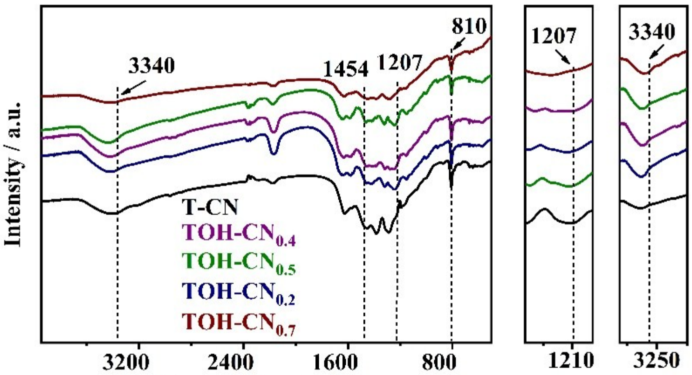

Figure S10. FTIR of T-CN, TOH-CN$_{0.2}$, TOH-CN$_{0.4}$, TOH-CN$_{0.5}$, TOH-CN$_{0.7}$.

In Figure S10, with the increase of oxygen content, the intensity of the NH$_x$ groups located at 1207 cm^{-1} in TOH-CN samples gradually decreased, and the intensity of the -OH groups located at 3340 cm^{-1} becomes increasingly apparent.

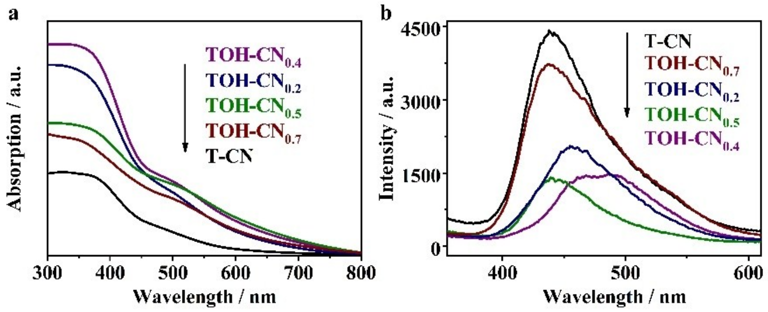

Figure S11. (a) UV-vis absorption, (b) PL emission spectra of T-CN, TOH-CN$_{0.2}$, TOH-CN$_{0.4}$, TOH-CN$_{0.5}$, TOH-CN$_{0.7}$.

As shown in Figure S11a, compared with T-CN, an obvious red shift in the 455–800 nm regions can be observed for the TOH-CN$_{0.2}$ and TOH-CN$_{0.4}$ as the increase of the oxygen content, indicating that the oxygen substitution results in a narrower bandgap associating with the introduction of interband states.[4,5] This effect is also corroborated by the PL spectra (Figure S11b), where the emission peak of TOH-CN$_{0.2}$ and TOH-CN$_{0.4}$, red-shifts in comparison to that of T-CN. Further increasing the amount of oxygen content led to a decrease in the absorption ability and increased PL intensity, which can be ascribed to the excess amount of introduced O atoms leading to the loss of heterostructure,[1] and a low degree of polymerization with reduce charge separation efficiency, respectively.[6] As a result, the photocatalytic H_2 evolution rate (Figure 4a) for the TOH-CN samples increased first, and then decreased, following the order TOH-CN$_{0.4}$ (2027.9 µmol g^{-1} h^{-1}) > TOH-CN$_{0.5}$ (1818.8 µmol g^{-1} h^{-1}) > TOH-CN$_{0.2}$ (1186.8 µmol g^{-1} h^{-1}) > TOH-CN$_{0.7}$ (884.0 µmol g^{-1} h^{-1}).

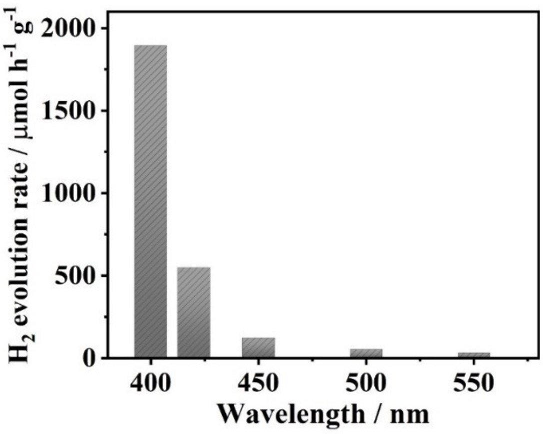

Figure S12. The H_2 evolution rate of TOH-CN$_{0.4}$ under difference irradiation wavelength.

Table S4. A summary of typical triazine-heptazine heterostructural carbon nitride photocatalysts and carbon nitride-based bifunctional photocatalysts reported for H_2 evolution rate, O_2 evolution rate and AQY for HER. (N/A means no report).

	Photo-catalysts	**Co-catalyst**	**Sacrificial agent**	**Light source**	**H_2 evolution rate** (µmol h^{-1} g^{-1})	**O_2 evolution rate** (µmol h^{-1} g^{-1})	**AQY for HER**	**Ref.**
	TOH-$CN_{0.4}$	Pt/CoO_x	Methanol/ $NaIO_3$	λ≥420 nm	2027.9	142.5	7.9% (420 nm)	This work
CN-based bifunctional photocatalysts	Pt/CNSC	Pt	TEOA	λ>300 nm	41.5	21.3	0.43% (420 nm)	[7]
	(Cring)-C_3N_4	Pt	Without	λ≥420 nm	371	184	5% (420 nm)	[8]
	C-PDA–g-C_3N_4	Pt/$AgNO_3$	TEOA	λ> 400 nm	810	56	2.3% (420 nm)	[9]
	CNU-$Br_{0.1}$	Pt/$AgNO_3$	TEOA	λ≥420 nm	960	20	N / A	[10]
	FAT-1.0	Pt/$NaNO_3$	TEOA	λ≥420 nm	772	145	8.6% (420 nm)	[1]
triazine-heptazine heterostructural CN photocatalysts	MS-550	Pt	TEOA	λ≥420 nm	661	N / A	2.88% (420 nm)	[11]
	HTCN-500	Pt	TEOA	λ≥420 nm	890	N / A	26.7% (420 nm)	[12]
	mw-ms-g-C_3N_4	Pt	TEOA	λ≥420 nm	1480	N / A	10.7% (420 nm)	[13]

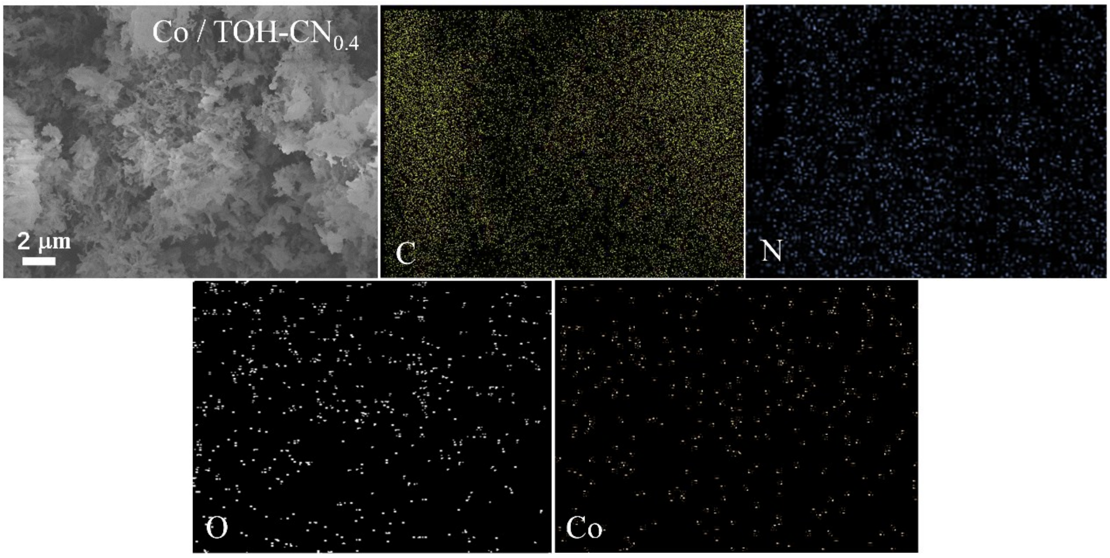

Figure S13. SEM image and the corresponding EDX element mappings of the Co/TOH-$CN_{0.4}$, showing the distribution of C, N, O, Co.

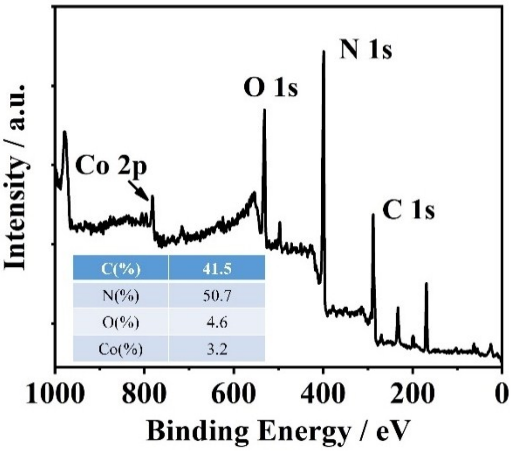

C(%)	41.5
N(%)	50.7
O(%)	4.6
Co(%)	3.2

Figure S14. XPS spectra of the Co/TOH-$CN_{0.4}$.

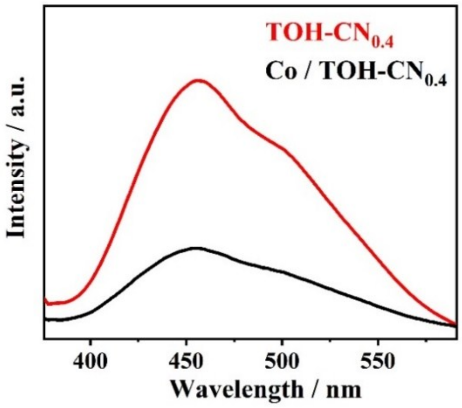

Figure S15. The PL spectrum of TOH-$CN_{0.4}$ and Co/ TOH-$CN_{0.4}$.

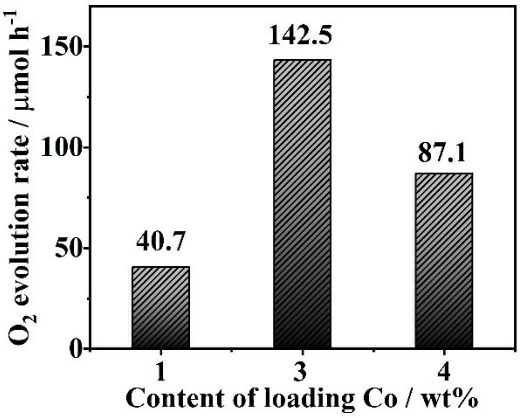

Figure S16. Photocatalytic O_2 evolution activities of the TOH-$CN_{0.4}$ loaded with different amount of Co species cocatalyst under visible irradiation (λ＞420 nm).

References

1 Y. Wang, F. Silveri, M. K. Bayazit, Q. Ruan, Y. Li, J. Xie, C. R. A. Catlow and J. Tang, *Adv. Energy Mater.*, 2018, **8**, 1801084.

2 K. Schwinghammer, M. B. Mesch, V. Duppel, C. Ziegler, J. r. Senker and B. V. Lotsch, *J. Am. Chem. Soc.*, 2014, **136**, 1730-1733.
3 J. Liu, J. Ke, Y. Li, B. Liu, L. Wang, H. Xiao and S. Wang, *Appl. Catal., B*, 2018, **236**, 396−403.
4 Z. F. Huang, J. Song, L. Pan, Z. Wang, X. Zhang, J.-J. Zou, W. Mi, X. Zhang and L. Wang, *Nano Energy*, 2015, **12**, 646-656.
5 L. Ming, H. Yue, L. Xu and F. Chen, *J. Mater. Chem. A*, 2014, **2**, 19145-19149.
6 Q. Han, F. Zhao, C. Hu, L. Lv, Z. Zhang, N. Chen and L. Qu, *Nano Res.*, 2015, **8**, 1718-1728.
7 Y. Zeng, H. Li, J. Luo, J. Yuan, L. Wang, C. Liu, Y. Xia, M. Liu, S. Luo and T. Cai, *Appl. Catal., B*, 2019, **249**, 275–281.
8 W. Che, W. Cheng, T. Yao, F. Tang, W. Liu, H. Su, Y. Huang, Q. Liu, J. Liu and F. Hu, *J. Am. Chem. Soc.*, 2017, **139**, 3021–3026.
9 F. He, G. Chen, Y. Yu, Y. Zhou, Y. Zheng and S. Hao, *Chem. Commun.*, 2015, **51**, 6824–6827.
10 Z.-A. Lan, G. Zhang and X. Wang, *Appl. Catal., B*, 2016, **192**, 116–125.
11 J. Yang, Y. Liang, K. Li, G. Yang, K. Wang, R. Xu and X. Xie, *Appl. Catal., B*, 2020, **262**, 118252.
12 Y. Li, F. Gong, Q. Zhou, X. Feng, J. Fan and Q. Xiang, *Appl. Catal., B*, 2019, 118381.
13 H. Liu, D. Chen, Z. Wang, H. Jing and R. Zhang, *Appl. Catal., B*, 2017, **203**, 300–313.